Cr_2O_3 nanoparticles boosting Cr–N–C for highly efficient electrocatalysis in acidic oxygen reduction reaction

Tao Jiang,[a] Weiling Luan,[a,*] Lyudmila Turyanska,[b] and Qi Feng[c]

[a] School of Mechanical and Power Engineering, Key Laboratory of Pressure Systems and Safety (MOE), East China University of Science and Technology, Shanghai, 200237, P. R. China, E-mail: luan@ecust.edu.cn

[b] Faculty of Engineering, University of Nottingham, NG72RD, UK

[c] Prospective Technology Department, SAIC Motorcycle Company, Shanghai 201800, China

Abstract: Transition metal–nitrogen–carbon (M–N–C) catalysts have attracted significant attention for catalyzing oxygen reduction reactions (ORR). In this study, a porous Cr_2O_3@Cr–N–C catalyst with a small amount of Cr_2O_3 nanoparticles loaded on the surface of $Cr–N_4–C$ nanomaterials was prepared using synergistic heat treatment (SHT) method with zeolite imidazole frameworks (ZIFs) as precursors. TEM and spherical aberration-corrected TEM results demonstrated the presence of hollow morphologies, Cr_2O_3 nanoparticles and atomic-level Cr distribution in Cr_2O_3@Cr–N–C. XPS, XRD and XAFS analysis indicated the coexistence of Cr_2O_3 nanoparticles and $Cr–N_4$ sites which were believed to act as active centers for ORR. In 0.1 M $HClO_4$, this material showed outstanding ORR catalytic activity with a half-wave potential of 0.78 V that was 40 mV higher than the traditional heat treatment derived Cr–N–C. It also

revealed relatively low Tafel slope of 52.2 mV dec^{-1}; 4-electron pathway; remarkable

stability and long-term durability. The improved ORR performance is mainly attributed

to the synergy between Cr–N$_4$ active center and Cr$_2$O$_3$ nanoparticle. The SHT strategy

reported here provides a new route to prepare highly efficient non-precious metal

M−N−C catalysts with greater ORR activity and stability in acidic environments.

Keywords: Cr$_2$O$_3$ • Cr–N−C • nanoparticle • oxygen reduction • catalyst

1. Introduction

In recent years, development of fuel cells has attracted significant attention worldwide

owing to high efficiency and zero emissions [1-4]. Proton exchange membrane fuel

cells (PEMFCs) require the use of acidic media at room temperature and have been

widely considered as a potential energy source for future vehicles [5-7]. However, the

reaction kinetics of the cathodes in PEMFCs are sluggish; therefore, the development

of inexpensive and efficient oxygen reduction reaction (ORR) catalysts must be

fabricated for further applications of PEMFCs [8]. Extensive efforts have been

undertaken to prepare transition metal (e.g., Fe, Co, Mn and Cu) -based ORR catalysts

[2, 9-12] with particular focus on developing rational design of the catalyst to achieve

enhanced performance [12]. Nitrogen sites are known to play important roles in the

catalysis of ORR in the presence of transition metal and N co-doped nanocarbon (M-

N-C) materials [13-15]. Recently, Fe–N–C species are proposed as promising

alternatives to commercial precious metal Pt-based catalysts for PEMFC [16-18]. The

catalytic performance analyses of Fe–N–C in both acidic and alkaline electrolytes was comparable to the known Pt/C catalyst [19-21]. However, the Fenton effect hinders the practical application of Fe–N–C, as well as the solubility of the Fe–N$_x$ sites in the presence of an acidic medium [22-25]. Therefore, other transition metal-based catalysts have been considered, such as Co–N–C, Mn–N–C, and Mg–N–C, which show enhanced catalytic performance for ORR in acidic media [26-29].

The performance of M–N–C-based ORR catalysts usually depend on their porosity, metal distribution, and N coordination [30, 31]. The presence of micropores in catalysts provides more exposure sites for active centers. Moreover, formation of mesopores results in high specific surface area and provides channels for reactants, such as O$_2$. On the other hand, macropores and hollow structures promote the discharge of reaction products (e.g., water) and accelerate the reaction [32-34]. It is noteworthy that hierarchical porous nanocarbon materials, which include at least two types of pores, have been confirmed to display superior catalytic activity compared to single pore size distribution species [35]. Metal–organic–frameworks (MOFs) are porous nanomaterials composed of transition metals and a rich carbon matrix. MOFs are widely used as precursors for ORR catalysts [36-38]. The M–N–C catalysts are generally synthesized using pyrolysis process at high temperatures (> 700°C). At such temperatures, transition metals, particularly Co and Fe, easily aggregate into clusters, hindering the transport of reactants and decreasing the exposure rate of active sites, which significantly deteriorates the catalytic performance [14, 39]. Additionally, catalysts with single-atom distribution have attracted significant interest owing to their maximum utilization of

3

metal sites and excellent catalytic performance [40-42]. Notably, the ORR activity of N-doped nanocarbon materials strongly depends on N coordination. For instance, pyridinic N, metallic N and graphitic N species have been observed after the pyrolysis of transition metal doped zeolite imidazole frameworks (M-ZIFs), and such moieties generally promote the ORR activity [43-47]. Cr–N–C species typically exhibit properties comparable to Fe–N–C and Mn–N–C. However, Cr–N–C and its ORR activity has not been extensively investigated or compared with commercial Pt-based catalysts [18, 41, 48, 49]. Despite a body of work, there is still a strong need for development of precious metal free catalysts with high ORR activity and stability in harsh environments.

Here we report on successful preparetion of a porous Cr_2O_3@Cr–N–C catalyst with a small amount of Cr_2O_3 nanoparticles loaded on the surface of Cr–N_4–C nanomaterials employing a previously reported synergistic heat treatment (SHT) method with minor modifications [32]. In a 0.1 M $HClO_4$ electrolyte, the half-wave potential ($E_{1/2}$) of the as-prepared Cr_2O_3@Cr–N–C catalyst was determined at 0.78 V *vs.* RHE. Notably, this value is much superior to that of a traditional heat treatment derived Cr–N–C sample and only 80 mV lower than that of Pt/C catalyst. The improved ORR activity of the catalyst was mainly attributed to the introduction of Cr_2O_3 nanoparticles, which enhanced the favorable synergy between and Cr–N_4 active sites and Cr_2O_3 nanoparticles.

2. Experimental Section

2.1. Chemicals

Ethanol and methanol were purchased from Titan (Shanghai, China). Isopropanol, perchloric acid ($HClO_4$), chromium trichloride hexahydrate ($CrCl_3 \cdot 6H_2O$), zinc nitrate hexahydrate ($Zn(NO_3)_2 \cdot 6H_2O$), and cobalt nitrate hexahydrate ($Co(NO_3)_2 \cdot 6H_2O$) were obtained from Adamas Pharmaceuticals (Emeryville, CA, USA). Dimethylimidazole (MeIM) was purchased from Kuer Chemical (Beijing, China). Membrane-solution Nafion (5%) and commercial Pt/C 20 wt% catalysts were purchased from Hesen (Shanghai, China). All chemicals were used as received.

2.2. Synthesis of Cr−ZIF-8

ZIF-8 was synthesized by adding 40 mL of a methanol solution containing 3.0 g of $Zn(NO_3)_2 \cdot 6H_2O$ into 80 mL of a methanol solution containing 6.5 g of MeIM. The reaction mixture was stirred for 24 h at room temperature and then dried at 60 °C in a vacuum oven. Furthermore, ZIF-67 was prepared by adding 500 mL of a methanol solution containing 7.28 g of $Co(NO_3)_2 \cdot 6H_2O$ into 500 mL of a methanol solution containing 12.19 g of MeIM. The reaction mixture was stirred for 24 h at room temperature and then dried at 60 °C in a vacuum oven. 100 mg of as-prepared ZIF-8 was dissolved in 15 mL of ethanol under sonication for 15 min. Subsequently, 7.5 mg of $CrCl_3 \cdot 6H_2O$ (50 mg mL^{-1} aqueous solution) was added to the solution under sonication for 20 min (2.5 mg and 12.5 mg $CrCl_3 \cdot 6H_2O$ for low Cr and high Cr sample, respectively). The mixture was stirred for 24 h at room temperature and then washed two times with ethanol. The crude product was collected following drying at 60 °C in a vacuum oven to form green powder of Cr–ZIF-8.

2.3. Preparation of catalysts

To prepare the catalyst, 150 mg of ZIF-67 and 100 mg of Cr–ZIF-8 were added into two ceramic boats placed next to each other in a tube furnace [32]. Cr–ZIF-8 was placed on the inlet side. After exhausting the air in the quartz tube for 2 h at an Ar atmosphere, the above two samples were calcined at 900 °C (800 °C, 1000 °C) for 2 h at a heating speed of 5 °C min^{-1}. The product based on Cr–ZIF-8 was denoted as Cr_2O_3@Cr–N–C. For comparison, Cr–N–C was prepared by directly calcining Cr–ZIF-8 under the same conditions.

2.4. Characterization

Transition electron microscopy (TEM) (JEOL JEM-2100F) was used to investigate the morphology of the samples. Aberration-corrected transmission electron microscopy (ACTEM) (FEI Titan Themis TEM) was employed to evaluate the atomic-level distribution of Cr in Cr_2O_3@Cr–N–C. HAADF-STEM imaging and electron energy loss spectroscopy analyses were carried out using Tecnai G2 F20 S-TWIN. X-ray diffraction (XRD) (Rigaku 2550VB) patterns were used to analyze the crystallization characteristics of the samples. X-ray photoelectron spectroscopy (XPS) (Thermo ESCALAB250) spectra were employed to investigate the chemical structure of the materials. Raman spectra (LabRAM HR, JY-Evolution, 532 nm) were used to evaluate the graphitization degree of the obtained samples. X-ray absorption fine spectroscopy (XAFS) was used to analyze the fine coordination of Cr. (See Supplementary Material, SI1 for details.)

2.5. Electrochemical measurements

All catalytic performance tests were based on a three-electrode system. The catalyst

inks were prepared as follows: 5 mg of $Cr_2O_3@Cr–N–C$ or $Cr–N–C$ was dispersed in

470 μL of ethanol, 470 μL of water, and 60 μL of Nafion prior to ultrasonication for 1

h. The commercial Pt/C catalyst ink was prepared by dispersing 4 mg of Pt/C and 13

μL of Nafion in 715 μL of water and 285 μL of isopropanol by ultrasonication for 30

min. The working electrodes were composed of a glass carbon electrode with a rotating

disk electrode (RDE) having 5-mm diameter and a rotating ring-disk electrode (RRDE)

having 4-mm disk and 1-mm ring diameters. A silver/silver chloride (Ag/AgCl)

electrode was used as the reference electrode, while a graphite rod electrode was the

counter electrode. Different loadings of $Cr_2O_3@Cr–N–C$ (i.e., 0.1, 0.2, 0.4, 0.6, and 0.8

mg cm^{-2} corresponding to 2.5, 5, 10, 15, and 20 μL of catalyst inks on RRDE,

respectively) were investigated. A 0.1 M $HClO_4$ solution was used as the electrolyte in

all tests. The cyclic voltammetry (CV) curves were obtained in an O_2-saturated 0.1 M

$HClO_4$ solution at potential ranges from −0.28 to 1.0 V at a scanning rate of 50 mV s^{-1}.

The linear sweep voltammetry (LSV) curves were acquired in an O_2-saturated 0.1 M

$HClO_4$ solution at potential ranges from −0.2 to 1.0 V at a scanning rate of 5 mV s^{-1}.

The electron transfer number, n, could be calculated using the Koutecky–Levich (K–L)

equations [32]. The n value and H_2O_2 yield are calculated according to the RRDE results

and related equations. The collection efficiency (0.39) of the ring electrode measured

in 1 M potassium ferricyanide ($K_3Fe(CN)_6$) and 0.1 M KCl solutions [32]. The ring

electrode potential was 1.48 V (*vs.* RHE).

3. Results and Discussion

3.1. Microscopic characterization of catalysts

To synthesis the $Cr_2O_3@Cr-N-C$ catalyst we used a modified synergistic heat treatment process [32], with ZIF-67 and Cr–ZIF-8 as precursors. In this method, the presence of ZIF-68 directly affects the chemical structure, the pore distribution and the number of active sites, hence enhancing the ORR performance [32]. The morphologies and components of $Cr_2O_3@Cr-N-C$ were investigated by electron microscopy. TEM images as shown in Fig. 1a demonstrated the existence of porous morphology in $Cr_2O_3@Cr-N-C$, including some hollows (or macropores) with a size of approximately 100 ± 50 nm. The high-angle annular dark-field scanning transmission electron microscopy (HAADF-STEM) image in Fig. 1b and Fig. 1c (magnified field) displayed evident bright particles sized approximately 10 nm. Furthermore, the high-resolution TEM image of this particle indicates that the lattice spacing was 0.25 nm, corresponding to (110) plane of Cr_2O_3 (top of Fig. 1c). The spherical aberration-corrected transmission electron microscopy (ACTEM) analysis was conducted to analyze the atomic distribution of Cr, as shown in Fig. 1d. The numerous isolated bright dots in magnified region (Fig. 1e) corresponded to Cr atoms, indicating the atomic-level distribution of this metal. The elemental maps of $Cr_2O_3@Cr-N-C$ suggested a uniform distribution of N and Cr in the carbon matrix (Fig. 1f, Fig. S1), indicating the possible existence of coordinated $Cr-N_x$ complexes. Unlike for SHT produced structured, the TEM and high-resolution TEM images of Cr–N–C showed the lack of hollow morphologies and nanoparticles (Fig. S2, Fig. S3). The N_2 adsorption-desorption curve of $Cr_2O_3@Cr-N-$ C corresponded to a type IV isotherm, suggesting the existence of mesopores (Fig. 2a).

Furthermore, Cr_2O_3@Cr–N–C exhibited an obvious uptake at lower relative pressure, which implied the presence of micropores. It also displayed a typical H3-type hysteresis loop at a relative pressure of approximately 0.4, which was attributed to the existence of mesopores [50]. The corresponding pore size distribution, shown in the insert of Fig. 2a, further suggested the presence of both micropores and mesopores. Moreover, the isotherm curve and corresponding pore size distribution of Cr–N–C were analogously investigated. The specific surface area and average pore size of Cr_2O_3@Cr–N–C were established at 1145 g cm^{-2} and 6.37 nm, respectively, larger than those of Cr–N–C (1052 g cm^{-2} and 4.23 nm, respectively). In addition, the pore volume of Cr_2O_3@Cr–N–C was determined at 1.82 cm^3 g^{-1}, which was also considerably larger than that of Cr–N–C (1.13 cm^3 g^{-1}). Hence, the SHT-derived hollow porous Cr_2O_3@Cr–N–C catalyst exhibited a larger specific surface area and pore volume than Cr–N–C, which can positively affect the current density in ORR. The composition of the catalyst is also an important factor affecting its activity. As shown in Fig. 2b, the Raman spectra of Cr_2O_3@Cr–N–C revealed two peaks at 1345 and 1580 cm^{-1}, corresponding to the disordered (D) and graphitic carbon (G), respectively. The ratio of these peaks, I_G/I_D, is used to measure the degree of graphitization of carbon materials. The value was calculated at 1.18 for Cr_2O_3@Cr–N–C which was higher than that of Cr–N–C (1.10), indicating SHT method enhanced the graphitization degree of ZIF-based precursors [32]. The X-ray diffraction (XRD) patterns demonstrated in Fig. 2c indicated three obvious peaks at 24.5, 33.6, and 36.2°, which were attributed to Cr_2O_3 (PDF#70-3766) in Cr_2O_3@Cr–N–C. However, Cr signals were not detected in Cr–N–C sample. In

addition, it is noteworthy that no peaks corresponding to metallic Cr were detected in the spectrum of the low Cr sample. Conversely, enhanced peaks associated with Cr_2O_3 were observed in the pattern of the high Cr sample (Fig. S4). These results implied that Cr_2O_3 particles were successfully formed using the SHT method. The Cr content in the samples was investigated using inductively coupled plasma (ICP) spectroscopy and the results were summarized in Table S1, $Cr_2O_3@Cr–N–C$ exhibited a similar Cr content (2.08 wt%) as Cr–N–C (2.03 wt%).

3.2. Identification of active sites

To evaluate the chemical state and coordination of Cr in $Cr_2O_3@Cr–N–C$ and Cr–N–C, X-ray photoelectron spectroscopy (XPS) was conducted as shown in Fig. S5 and Fig. S6, respectively. High-resolution XPS spectra were used to examine the coordination states of C, N, and Cr (Fig. 2d). Three C 1s peaks were observed at 284.6, 285.7, and 287.0 eV, corresponding to C–C (C_1), C–N (C_2), and C=N (C_3), respectively. The existence of C–N and C=N indicated successful doping of N into the carbon matrix. It is known that the type of N coordination significantly affects ORR. Four peaks observed at 398.4, 399.7, 400.5, and 401.9 eV in Fig. 2e were attributed to pyridinic N (N_1), Cr–N_x (N_2), graphitic N (N_3), oxidized N (N_4) and oxidized pyridinic N (N_5), respectively [25]. As shown in Fig. 2f, the obtained data suggested similar N_2, N_3 and N_4 contents in $Cr_2O_3@Cr–N–C$ and Cr–N–C. However, significantly higher N_5 and N_1 contents were observed in $Cr_2O_3@Cr–N–C$ and Cr–N–C, respectively. This implies that after the SHT process, N_1 in Cr–N–C was transformed into N_5 in $Cr_2O_3@Cr–N–C$ and coordinated with Cr to form the Cr_2O_3 nanoparticles. The higher N_3 content in

Cr$_2$O$_3$@Cr–N–C compared to Cr–N–C was further confirmed by our Raman spectroscopy studies, which revealed higher graphitization degree associated with greater catalyst stability in ORR. The Cr 2p spectra of Cr$_2$O$_3$@Cr–N–C are illustrated in Fig. S7. Obviously, two obvious split peaks were observed at 576.95 eV and 586.2 eV, corresponding to Cr$_2$O$_3$ 2p 3/2 and Cr$_2$O$_3$ 2p 1/2, respectively.

To further analyze the chemical state of Cr in Cr$_2$O$_3$@Cr–N–C, X-ray absorption fine spectroscopy (XAFS) was conducted. The Fourier-transformed k3-weighted extended X-ray absorption fine structure (FT-EXAFS) spectra of Cr$_2$O$_3$@Cr–N–C and its counterparts (Cr foil and Cr$_2$O$_3$) are shown in Fig. 3a and Fig. 3b, respectively. The dominant fitted peak at 1.54 Å corresponds to Cr–N/Cr–O and the second-shell peak at 2.52 Å corresponding to Cr–O–Cr were observed. As the close position of N and O in the periodic table, it is difficult to distinguish Cr–N and Cr–O through the R space presented by FT-EXAFS spectra. Therefore, wavelet-transform (WT) EXAFS analysis was conducted, as shown in Fig. 3c and Fig. 3d. Cr$_2$O$_3$@Cr–N–C showed a WT-maximum at the k value of 3.9 Å^{-1} which was a little higher than that of pure Cr–N (3.8 Å^{-1}) and much lower than that of Cr$_2$O$_3$ reference (4.2 Å^{-1}). Thus, the tiny positive shift of the WT-maximum in Cr$_2$O$_3$@Cr–N–C compared to pure Cr–N was attributed to the introduction of Cr–O (Cr$_2$O$_3$). As shown in Fig. 3e, the Cr k-edge X-ray absorption near edge structure (XANES) results indicated that the pre-edge position of Cr$_2$O$_3$@Cr–N–C was far positive than Cr foil and very close to Cr$_2$O$_3$, which confirmed that the valence state was close but slightly below +3. Thus, we deduce that both Cr–N with Cr^{2+} and Cr$_2$O$_3$ with Cr^{3+} exist in Cr$_2$O$_3$@Cr–N–C through

the above fine coordination analysis and valence state results. The presence of Cr–N

and the absent of Cr–Cr were consistent with the ACTEM results, indicating the atomic-

level distribution of Cr–N_x active sites. Moreover, the EXAFS fitting results showed

that Cr was coordinated by 5.3 (±0.3) N or O atoms at a distance of 1.98 Å (Table S2).

Cr–N_4 coordinates have been confirmed by calcining Cr-doped ZIF-8, as reported in

previous literature [41]. Furthermore, the atomic ratio of Cr and O in Cr_2O_3 is 1:1.5.

Therefore, we propose the number of N and O should be 4 and 1.5, respectively,

verifying the coexistence of Cr–N_4 and Cr_2O_3 in Cr_2O_3@Cr–N–C. Based on the above

discussion, the simplified local structure of Cr_2O_3@Cr–N–C is presented in Fig. 3f with

Cr_2O_3 nanoparticle located on the surface of Cr–N_4–C nanomaterials.

3.3. ORR performance tests

The ORR activity of the samples was tested using a typical three-electrode system.

The investigation was conducted in an O_2-saturated 0.1 M $HClO_4$ solution. Initially, we

examined the CV curves (Fig. 4a), which indicated a peak potential of 0.78 V (*vs.* RHE)

for Cr_2O_3@Cr–N–C and 0.83 V for the commercial Pt/C catalyst. To determine the half-

wave potential ($E_{1/2}$) for ORR, the LSV curves were investigated according to Fig. 4b.

It was established that in an acidic electrolyte, Cr_2O_3@Cr–N–C exhibited an $E_{1/2}$ value

of 0.78 V, which was only 80 mV lower than that of the Pt/C catalyst (0.86 V). On the

other hand, the Cr–N–C sample displayed a weaker $E_{1/2}$ of 0.74 V, which was 40 mV

lower than that of Cr_2O_3@Cr–N–C. Moreover, the onset potential for Cr_2O_3@Cr–

N–C and Cr–N–C was determined at 0.86 V and 0.85 V respectively. In addition, Cr_2O_3@Cr–

N–C showed comparable limited current density (5.0 mA cm^{-2}) to Pt/C (5.5 mA cm^{-2}).

However, the limited current density of Cr_2O_3@Cr–N–C was much higher than that of Cr–N–C (4.0 mA cm^{-2}), indicating that SHT-derived hollow structure was beneficial for the transport of reactants, such as water and O_2, enhancing the ORR performance. To analyze the ORR kinetics of Cr_2O_3@Cr–N–C, the LSV curves were evaluated at various rotation speeds from 400 to 2500 rpm. The corresponding Koutecky–Levich (K–L) plots showed excellent parallelism and linearity which was consistent with the first-order reaction kinetics (Fig. 4c). The kinetic current (@0.7 V vs. RHE) of Cr_2O_3@Cr-N-C (9.1 mA/cm^2) was comparable to that of Pt/C (12.5 mA/cm^2, Fig. S9a), further confirming the outstanding ORR activity of Cr_2O_3@Cr-N-C. Furthermore, the obtained Tafel plots implied that Cr_2O_3@Cr–N–C exhibited the lowest Tafel slope (52.2 mV dec^{-1}) compared to Pt/C (74.1 mV dec^{-1}) and Cr–N–C (71.2 mV dec^{-1}), further demonstrating the enhanced ORR activity of the prepared catalyst in an acidic electrolyte, as shown in Fig. 4d. The recyclability of a catalyst without any significant loss in ORR activity is important for its practical application in devices such as fuel cells. In this work, the LSV curve of N–C derived from directly pyrolysis of ZIF-8 was also tested and revealed reduced ORR activity with $E_{1/2}$=0.39 V for N-C compared to Cr-N-C, indicating the positive role of Cr-N_4 as active sites (Supplementary Information Fig. S8). The ORR activity of the synthesized material was also compared with other previously reported M−N−C catalysts (Table S3). It was found that the Cr_2O_3@Cr–N–C catalyst obtained via the SHT method possessed comparable activity in acidic media [42, 51-56]. The number of transferred electrons in ORR is an important indicator of the catalyst performance. The current density curves of Cr_2O_3@Cr–N–C

and Pt/C acquired based on the RRDE are illustrated in Figs. S9b-d, while the corresponding number of transferred electrons and H_2O_2 yield are shown in Fig. 5a. The average number of transferred electrons at 0.1–0.8 V for Cr_2O_3@Cr–N–C was determined at 3.91, which was comparable to that for Pt/C (3.94). This result confirmed that the catalysis of ORR by Cr_2O_3@Cr–N–C in acidic media occurred via a direct four-electron pathway. Moreover, Cr_2O_3@Cr–N–C had a slightly higher average H_2O_2 yield (5.5%) than that observed in the case of Pt/C (4.2%), further indicating the direct four-electron pathway. Effective practical application of a catalyst generally requires good durability of the material. After 50,000 s, the results of the accelerated durability test of Cr_2O_3@Cr–N–C suggested a relative current of 90%. In contrast, for Pt/C, this value was established at only 50% (Fig. 5b). Furthermore, the TEM analysis and evaluation of the corresponding elemental maps of Cr_2O_3@Cr–N–C following long-term durability test indicated its superior structural stability (Fig. S10). Both the electrochemical durability and structural stability were beneficial for the potential of the as-prepared hollow porous catalyst for utilization in acidic environments. We also conducted methanol tolerance tests, as shown in the insert of Fig. 5b, 5 mL of 3 M methanol was added into the electrolyte (50 mL) over 1000 s. The Cr_2O_3@Cr–N–C catalyst displayed excellent methanol tolerance with negligible change in the current, unlike Pt/C where a sharp decrease in the current was observed. Moreover, the stability of this catalyst was tested in acidic media, as shown in Fig. 5c. Strikingly, a small decay of 20 mV in the $E_{1/2}$ was observed after 20,000 CV cycles in potential ranges of 0.6–1.0 V, confirming the robustness of this Cr_2O_3@Cr–N–C catalyst. The remarkable long-

term durability and stability are beneficial for the practical applications of the material in various devices, including fuel cells.

In the present study, we also obtained LSV curves of Cr_2O_3@Cr–N–C under different catalyst loadings (Fig. 5d). It was found that the ORR activity was enhanced when the loading was increased from 0.1, 0.2, 0.4 to 0.6 mg cm^{-2}, corresponding to changes in $E_{1/2}$ at 0.74, 0.76, 0.77 to 0.78 V, respectively. Notably, the ORR activity at the highest loading of 0.8 mg cm^{-2} exhibited a relatively low $E_{1/2}$ of 0.73 V. This was attributed to the hindered transport of the reactants resulting from the high loading, which decreased the catalytic activity.

The preparation of Cr_2O_3@Cr–N–C was also conducted at different temperatures as well as Cr and ZIF-67 contents. As shown in Fig. S11, the ORR activity of the samples obtained at 800 °C and 1000 °C exhibited $E_{1/2}$ values of 0.76 and 0.72 V, respectively. The observed enhancement in the $E_{1/2}$ and limited current density at a temperature increase from 800 °C to 900 °C might be attributed to the greater degree of graphitization degree. In contrast, it was speculated that the sharp decrease in the limited current density noted when the temperature rose from 900 °C to 1000 °C resulted from the collapse of the hollows at such high temperatures. The Cr and ZIF-67 content are expected to affect the ORR activity of Cr_2O_3@Cr–N–C during a SHT process. As demonstrated in Fig. S12, the samples displaying high and low Cr content exhibited $E_{1/2}$ of 0.74 and 0.56 V, respectively. The relatively low activity of the sample with a low Cr content further confirmed the significant role of the Cr–N$_4$ moieties as the active centers. Furthermore, the ORR activity of Cr_2O_3@Cr–N–C treated with

different ZIF-67 contents was inferior for both low and high ZIF-67 content samples, with $E_{1/2}$ of 0.67 and 0.63 V, respectively (Fig. S13). Hence, the optimal conditions for SHT should include a temperature of 900 °C, Cr content of 2.08 wt%, and a Cr–ZIF-8 to ZIF-67 ratio of 2:3. We propose that the synergistic heating of Cr-ZIF-8 with ZIF-67 promoted the formation of hollow structures, while the presence of Cr_2O_3 (confirmed by characterization of TEM, XRD, XPS and XAFS) contributed to enhanced ORR activity in the acidic environments.

4. Conclusions

In summary, we successfully prepared a porous Cr_2O_3@Cr–N–C catalyst for ORR using a SHT method. The coexistence of Cr_2O_3 nanoparticles and Cr–N_4 sites in Cr_2O_3@Cr–N–C after the SHT was confirmed through a complete characterization and analysis. The electrochemical measurements conducted in an acidic electrolyte, specifically 0.1 M $HClO_4$, indicated that the as-prepared Cr_2O_3@Cr–N–C catalyst displayed outstanding ORR activity, with $E_{1/2}$ of 0.78 V which was only 80 mV lower than Pt/C. Cr_2O_3@Cr–N–C catalyst also exhibited a remarkably low Tafel slope of 52.2 mV dec^{-1} and an ideal 4-electron pathway for acidic ORR. Pleasingly, the excellent stability, methanol tolerance and long-term durability of the catalyst enable its potential application in various devices, such as PEMFCs. The enhanced ORR performance is mainly attributed to the synergy between Cr_2O_3 nanoparticles and Cr–N_4 active centers. We believe that the described SHT strategy provides a valuable platform for the preparation of high-performance and low-cost ORR catalysts.

Reference

[1] M.K. Debe, Nature 486 (2012) 43–51.

[2] J. Li, M. Chen, D.A. Cullen, S. Hwang, M. Wang, B. Li, K. Liu, S. Karakalos, M. Lucero, H. Zhang, C. Lei, H. Xu, G.E. Sterbinsky, Z. Feng, D. Su, K.L. More, G. Wang, Z. Wang, G. Wu, Nat. Catal. 1 (2018) 935–45.

[3] Y. Chang, J. Zhao, S. Shahgaldi, Y. Qin, Y. Yin, X. Li, Int. J. Hydrogen Energy 45 (2020) 29904–16.

[4] F. Yu, T. Han, Z. Wang, Y. Xie, Y. Wu, Y. Jin, N. Yang, J. Xiao, S. Kawi, Int. J. Hydrogen Energy 46 (2021) 4283–300.

[5] A. Ly, T. Asset, P. Atanassov, J. Power Sources 478 (2020) 228516.

[6] X. Zhao, X. Yang, M. Wang, S. Hwang, S. Karakalos, M. Chen, Z. Qiao, L. Wang, B. Liu, Q. Ma, D.A. Cullen, D. Su, H. Yang, H.Y. Zang, Z. Feng, G. Wu, Appl. Catal., B 279 (2020) 119400.

[7] Z. Zhou, D. Qiu, S. Zhai, L. Peng, X. Lai, Appl. Energy 277 (2020) 115532.

[8] F. Xiao, G.L. Xu, C.J. Sun, I. Hwang, M. Xu, H.W. Wu, Z. Wei, X. Pan, K. Amine, M. Shao, Nano Energy 77 (2020) 105192.

[9] X. Wen, Q. Zhang, J. Guan, Coordin. Chem. Rev. 409 (2020) 213214.

[10] H. Liu, S. Yi, Y. Wu, H. Wu, J. Zhou, W. Liang, J. Cai, H. Xu, Int. J. Hydrogen Energy 45 (2020) 16105–13.

[11] M. Mooste, T. Tkesheliadze, J. Kozlova, A. Kikas, V. Kisand, A. Treshchalov, A. Tamm, J. Aruvali, J.H. Zagal, A.M. Kannan, K. Tammeveski, Int. J. Hydrogen Energy 46 (2021) 4365–77.

[12] X. He, S. Ruan, Y. Chen, J. Zhang, C. Liang, H. Huang, Y. Gan, W. Zhang, Y. Xia, Ionics 26 (2020) 5065–73.

[13] C. Hu, C. Yu, M. Li, X. Wang, Q. Dong, G. Wang, J. Qiu, Chem. Commun. 51 (2015) 3419–22.

[14] K. Wang, H. Chen, X. Zhang, Y. Tong, S. Song, P. Tsiakaras, Y. Wang, Appl. Catal., B 264 (2020) 264.

[15] Y. Huang, W. Liu, S. Kan, P. Liu, R. Hao, H. Hu, J. Zhang, H. Liu, M. Liu, K. Liu, Int. J. Hydrogen Energy 45 (2020) 6380–90.

[16] D. Lyu, Y.B. Mollamahale, S. Huang, P. Zhu, X. Zhang, Y. Du, S. Wang, M. Qing, Z.Q. Tian, P.K. Shen, J. Catal. 368 (2018) 279–90.

[17] L. Osmieri, R.K. Ahluwalia, X. Wang, H.T. Chung, X. Yin, A.J. Kropf, J. Park, D.A. Cullen, K.L. More, P. Zelenay, D.J. Myers, K.C. Neyerlin, Appl. Catal., B 257 (2019) 117929.

[18] X. Wei, X. Luo, H. Wang, W. Gu, W. Cai, Y. Lin, C. Zhu, Appl. Catal., B 263 (2020) 118347.

[19] G.A. Ferrero, K. Preuss, A. Marinovic, A.B. Jorge, N. Mansor, D.J.L. Brett, A.B. Fuertes, M. Sevilla, M.M. Titirici, ACS Nano 10 (2016) 5922–32.

[20] Y. Li, T. Liu, W. Yang, Z. Zhu, Y. Zhai, W. Gu, C. Zhu, Nanoscale 11 (2019) 19506–11.

[21] X. He, Y. Xia, C. Liang, J. Zhang, H. Huang, Y. Gan, C. Zhao, W. Zhang, Nanotechnology 30 (2019) 144001.

[22] X. Zhang, Y.B. Mollamahale, D. Lyu, L. Liang, F. Yu, M. Qing, Y. Du, X. Zhang, Z.Q. Tian, P.K. Shen, J. Catal. 372 (2019) 245–57.

[23] Y. Xu, M.J. Dzara, S. Kabir, S. Pylypenko, K. Neyerlin, A. Zakutayev, Appl. Surf. Sci. 515 (2020) 146012.

[24] Y. Li, K. Zang, X. Duan, J. Luo, D. Chen, J. Energy Chem. 55 (2021) 572–79.

[25] F. Wang, Y. Zhou, S. Lin, L. Yang, Z. Hu, D. Xie, Nano Energy 78 (2020) 105128.

[26] K. Liu, Z. Qiao, S. Hwang, Z. Liu, H. Zhang, D. Su, H. Xu, G. Wu, G. Wang, Appl. Catal., B 243 (2019) 195–203.

[27] G. Liang, J. Huang, J. Li, Y. Wu, G. Huang, Y.Q. Jin, H. Zeng, H. Zhang, J. Chen, Y. Jin, N. Wang, F. Xie, H. Meng, J. Electrochem. Soc. 167 (2020) 104502.

[28] S. Liu, Z. Li, C. Wang, W. Tao, M. Huang, M. Zuo, Y. Yang, K. Yang, L. Zhang, S. Chen, P. Xu, Q. Chen, Nat. Commun. 11 (2020) 938.

[29] X. Wang, X. Xi, G. Huo, C. Xu, P. Sui, R. Feng, X.Z. Fu, J.L. Luo, J. Energy Chem. 53 (2020) 49–55.

[30] U. Martinez, S. Komini Babu, E.F. Holby, H.T. Chung, X. Yin, P. Zelenay, Adv. Mater. 31 (2019) 1806545.

[31] H. Huang, Y. Chang, J. Jia, M. Jia, Z. Wen, Int. J. Hydrogen Energy 45 (2020) 28764–73.

[32] T. Jiang, W. Luan, Y. Ren, C. Fan, Q. Feng, L. Turyanska, Micropor. Mesopor. Mater. 305 (2020) 110382.

[33] Q. Wei, G. Zhang, X. Yang, R. Chenitz, D. Banham, L. Yang, S. Ye, S. Knights, S. Sun, ACS Appl. Mater. Inter. 9 (2017) 36944–54.

[34] X. Yang, Y. Wang, G. Zhang, L. Du, L. Yang, M. Markiewicz, J.Y. Choi, R. Chenitz, S. Sun, Appl. Catal., B 264 (2020) 118523.

[35] Y. Wang, J. Hao, J. Yu, H. Yu, K. Wang, X. Yang, J. Li, W. Li, J. Energy Chem. 45 (2020) 119–25.

[36] Q. Ren, H. Wang, X.F. Lu, Y.X. Tong, G.R. Li, Adv. Sci. 5 (2018) 1700515.

[37] X. Duan, N. Pan, C. Sun, K. Zhang, X. Zhu, M. Zhang, L. Song, H. Zheng, J. Energy Chem. 56 (2021) 290–98.

[38] J. Chen, J.L. Long, J. Mol. Catal. 31 (2017) 463–71.

[39] Y. Ding, W. Yang, S. Gao, W. Sun, C. Sun, Q. Li, ACS Appl. Energy Mater. 3 (2020) 1328–37.

[40] M. Wang, H. Ji, S. Liu, H. Sun, J. Liu, C. Yan, T. Qian, Chem. Eng. J. 393 (2020) 124702.

[41] E. Luo, H. Zhang, X. Wang, L. Gao, L. Gong, T. Zhao, Z. Jin, J. Ge, Z. Jiang, C. Liu, W. Xing, Angew. Chem. Int. Ed. 58 (2019) 12469–75.

[42] X. Xu, Z. Xia, X. Zhang, R. Sun, X. Sun, H. Li, C. Wu, J. Wang, S. Wang, G. Sun, Applied Catal., B 259 (2019) 118042.

[43] H. Jin, H. Zhou, W. Li, Z. Wang, J. Yang, Y. Xiong, D. He, L. Chen, S. Mu, J. Mater. Chem. A 6 (2018) 20093–99.

[44] S. Lai, L. Xu, H. Liu, S. Chen, R. Cai, L. Zhang, W. Theis, J. Sun, D. Yang, X. Zhao, J. Mater. Chem. A 7 (2019) 21884–91.

[45] W.L. Xin, K.K. Lu, D. Shan, Appl. Surf. Sci. 481 (2019) 313–18.

[46] J. Ding, S. Ji, H. Wang, H. Gai, F. Liu, B.G. Pollet, R. Wang, Chem. Commun. 55 (2019) 2924–27.

[47] X. Zhang, Z. Yang, Z. Lu, W. Wang, Carbon 130 (2018) 112–19.

[48] D. Liu, L. Fu, X. Huang, K. Liu, J. Li, H. Xie, H. Wang, Y. Tang, J. Electrochem. Soc. 165 (2018) F662–F70.

[49] X. Xu, Z. Xia, X. Zhang, H. Li, S. Wang, G. Sun, Nanoscale 12 (2020) 3418–23.

[50] Z. Yang, Y. Wang, M. Zhu, Z. Li, W. Chen, W. Wei, T. Yuan, Y. Qu, Q. Xu, C. Zhao, X. Wang, P. Li, Y. Li, Y. Wu, Y. Li, ACS Catal. 9 (2019) 2158–63.

[51] X. Liu, H. Liu, C. Chen, L. Zou, Y. Li, Q. Zhang, B. Yang, Z. Zou, H. Yang, Nano Res. 12 (2019) 1651–57.

[52] X. Wen, L. Bai, M. Li, J. Guan, ACS Sustain. Chem. Eng. 7 (2019) 9249–56.

[53] F. Xiao, G.L. Xu, C.J. Sun, M. Xu, W. Wen, Q. Wang, M. Gu, S. Zhu, Y. Li, Z. Wei, X. Pan, J. Wang, K. Amine, M. Shao, Nano Energy 61 (2019) 60–68.

[54] J. Li, X. Zhu, J. Wang, Z. Rui, S. Zhang, Y. Li, R. Ding, W. He, J. Liu, Z. Zou, ACS Appl. Nano Mater. 3 (2020) 742–51.

[55] Y. Han, Y.G. Wang, W. Chen, R. Xu, L. Zheng, J. Zhang, J. Luo, R.A. Shen, Y. Zhu, W.C. Cheong, C. Chen, Q. Peng, D. Wang, Y. Li, J. Am. Chem. Soc. 139 (2017) 17269–72.

[56] M. Xiao, H. Zhang, Y. Chen, J. Zhu, L. Gao, Z. Jin, J. Ge, Z. Jiang, S. Chen, C. Liu, W. Xing, Nano Energy 46 (2018) 396–403.

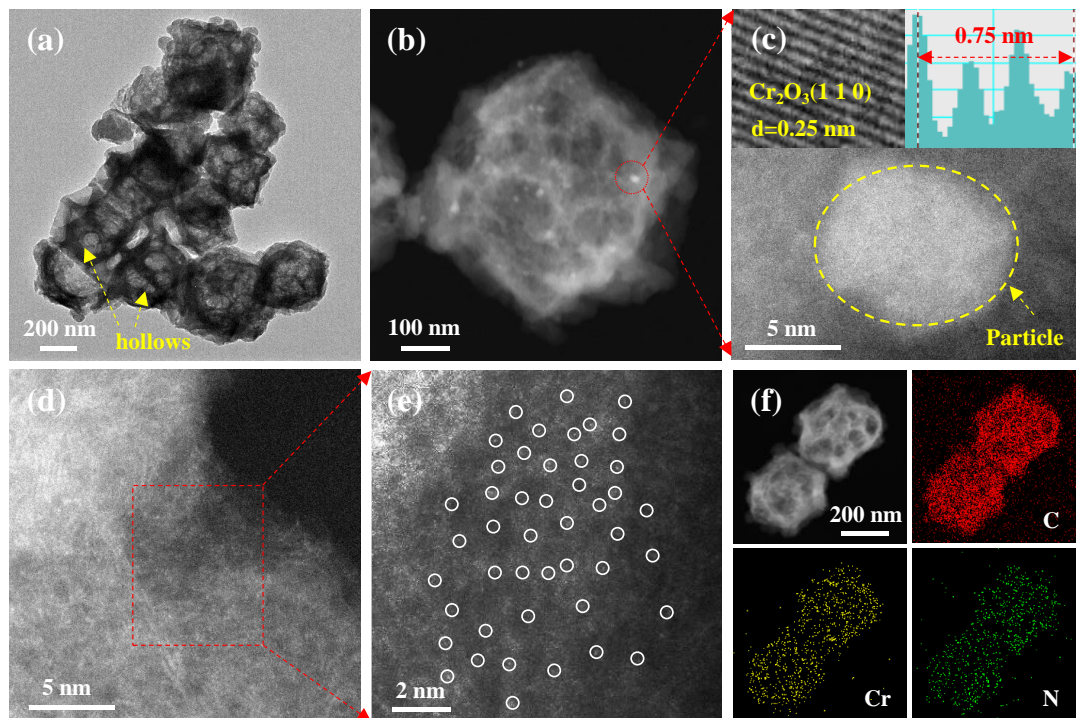**Fig. 1.** Electron microscope images of Cr_2O_3@Cr–N–C. (a) TEM, (b) HADDF-STEM and (c) magnified STEM and high-resolution TEM images of Cr_2O_3@Cr–N–C. (d) ACTEM and (e) its magnified image of Cr_2O_3@Cr–N–C. (f) The corresponding elemental mapping images of C, N and Cr.
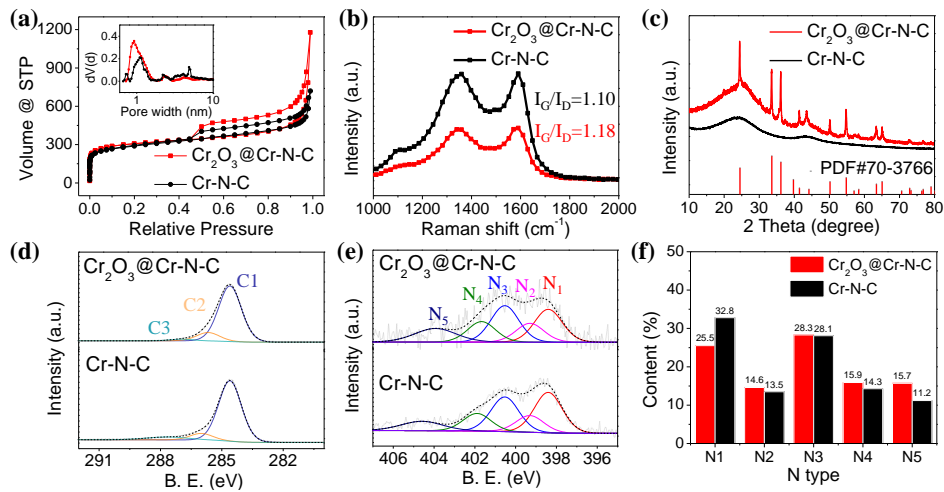
Fig. 2. (a) N_2 adsorption-desorption curve and corresponding pore size distribution of $Cr_2O_3@Cr-N-C$. (b) Raman shift spectra of $Cr_2O_3@Cr-N-C$. (c) XRD patterns of $Cr_2O_3@Cr-N-C$ and $Cr-N-C$. High resolution XPS spectra of (d) C 1s, (e) N 1s. (f) N content in $Cr_2O_3@Cr-N-C$ and $Cr-N-C$ samples.
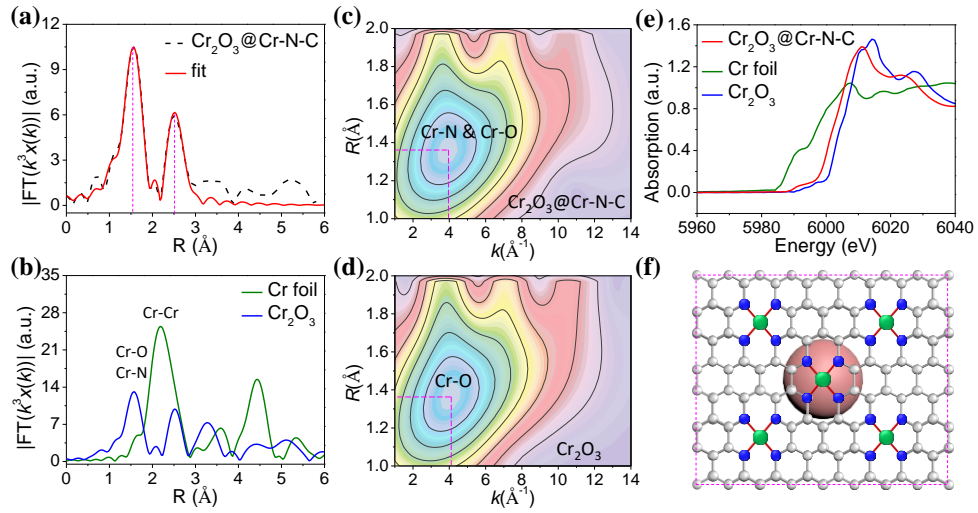
Fig. 3. Fine structure analysis. The k3-weighted Cr K-edge FT-EXAFS spectra of (a) Cr_2O_3@Cr–N–C and (b) Cr foil and Cr_2O_3 reference samples. WT-EXAFS plots of (c) Cr_2O_3@Cr–N–C and (d) Cr_2O_3 reference sample. (e) The normalized Cr K-edge XANES spectra of Cr_2O_3@Cr–N–C. (f) Schematic mode of Cr_2O_3@Cr–N–C.
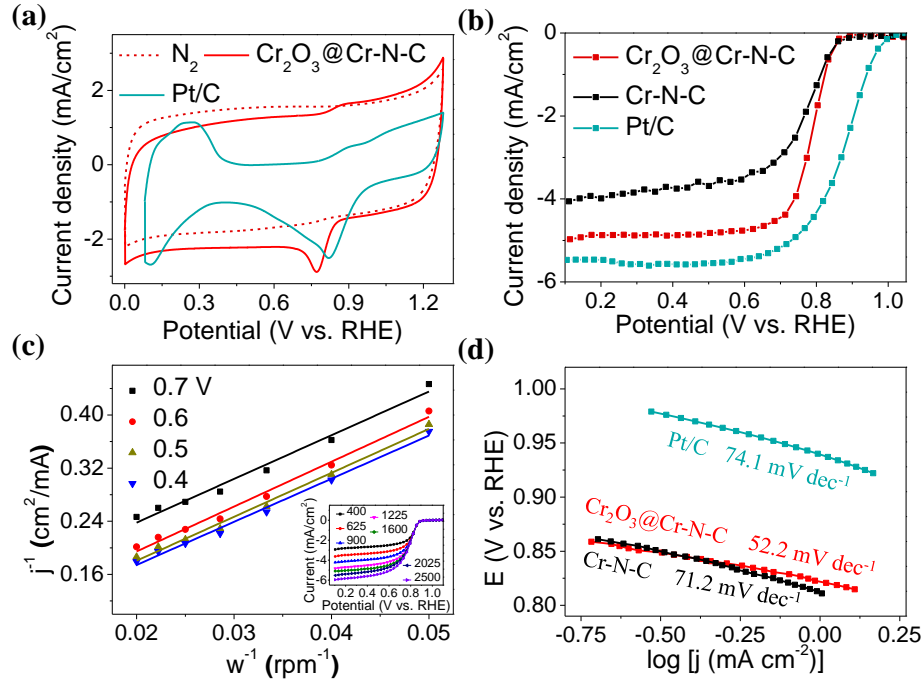
Fig. 4. Electrochemical performance analysis. (a) CV curves of Cr_2O_3@Cr–N–C and Pt/C catalysts. (b) LSV curves of Cr_2O_3@Cr–N–C, Cr−N−C and Pt/C catalysts. (c) K-L plots of Cr_2O_3@Cr–N–C catalyst from 0.4 to 0.7 V *vs.* RHE. (d) Tafel plots of Cr_2O_3@Cr–N–C, Cr−N−C and Pt/C catalysts. The dotted line in (a): CV curve of Cr_2O_3@Cr–N–C tested in N_2-saturated electrolyte. The insert in (c): LSV curves of Cr_2O_3@Cr–N–C tested at different rotation rate from 400 to 2500 rpm. The electrolytes for above tests are O_2-saturated 0.1 M $HClO_4$ solution and the rotation rate for (b) is 1600 rpm.
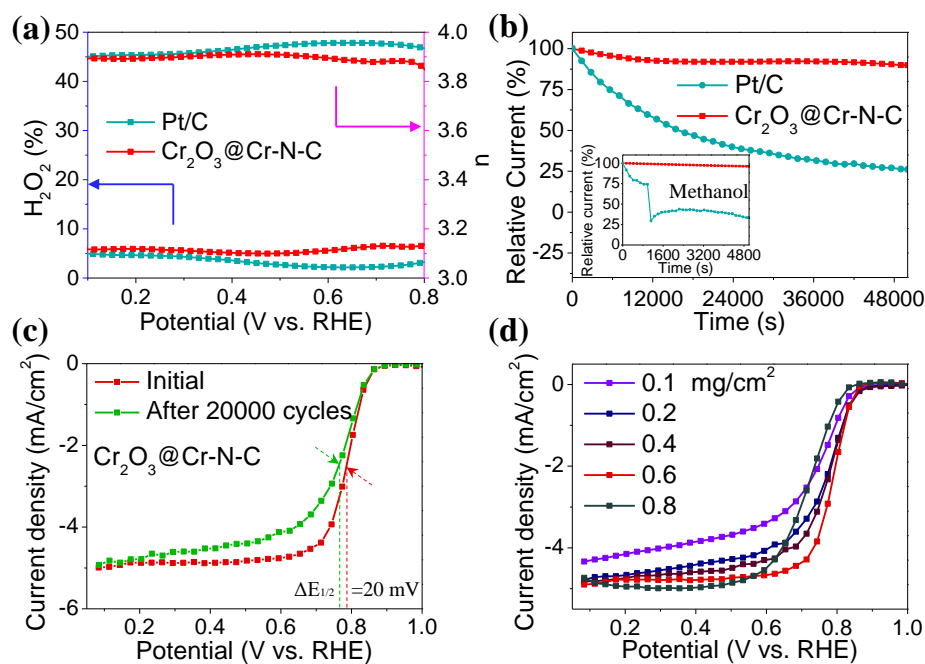
Fig. 5. (a) The number of electrons transferred and yield of H_2O_2 of Cr_2O_3@Cr–N–C and Pt/C during ORR. (b) Long-term durability tests of Cr_2O_3@Cr–N–C and Pt/C at 0.7 V *vs.* RHE with rotation rate of 900 rpm. (c) LSV curves of Cr_2O_3@Cr–N–C before and after 20,000 CV cycles. (d) LSV curves of Cr_2O_3@Cr–N–C with different catalyst loading from 0.1 to 0.8 mg cm^{-2}. The insert in (b): methanol tolerance tests of Cr_2O_3@Cr–N–C and Pt/C at 0.7 V *vs.* RHE with rotation rate of 1600 rpm.